JOURNAL OF AIRCRAFT
Vol. 46, No. 1, January–February 2009

Numerical Simulation of Maneuvering Aircraft by Aerodynamic, Flight-Mechanics, and Structural-Mechanics Coupling

Andreas Schütte,* Gunnar Einarsson,† Axel Raichle,† Britta Schöning,† and Wulf Mönnich‡
DLR, German Aerospace Center, D 38108 Brunswick, Germany
Matthias Orlt,§ Jens Neumann,¶ and Jürgen Arnold¶
DLR, German Aerospace Center, D 37073 Göttingen, Germany
and
Tomas Forkert**
DLR, German Aerospace Center, D 51147 Cologne, Germany

DOI: 10.2514/1.31182

Selected results of the DLR project Simulation of Complex Maneuvers are presented. The objective of this project is to develop and validate a numerical tool to simulate the unsteady aerodynamics of a free-flying aeroelastic combat aircraft, by use of coupled aerodynamic, flight mechanics, and aeroelastic computations. To achieve this objective, the unstructured, time-accurate flow-solver TAU is coupled with a computational module solving the flight-mechanics equations of motion and a structural-mechanics code determining the structural deformations. The numerical results are validated by experimental data. For this purpose, several specific wind-tunnel experiments with different wind-tunnel models are carried out.

Nomenclature

$c_L = L/(q_\infty \cdot F)$	=	lift coefficient
$c_l = l/(q_\infty \cdot F \cdot l_\mu)$	=	roll-moment coefficient
$c_M = M/(q_\infty \cdot F \cdot l_\mu)$	=	pitching-moment coefficient
$c_p = (p - p_\infty)/q_\infty$	=	pressure coefficient
dy	=	deformation increment in y direction
dz	=	deformation increment in z direction
F	=	reference area
f	=	frequency
l_i	=	chord length of the model
l_μ	=	aerodynamic mean chord
M_x	=	rolling moment
M_y	=	pitching moment
M	=	Mach number
$q_\infty = \rho_\infty/2 \cdot V_\infty^2$	=	dynamic pressure coefficient
$Re = V_\infty \cdot l_i/\nu$	=	Reynolds number
t	=	time
V_∞	=	on-flow velocity
α	=	angle of attack
Δt	=	physical time step size
$\Delta\alpha$	=	angle-of-attack amplitude
η	=	flap deflection angle
Θ	=	incidence angle, pitch angle at $\Phi =$ 0 deg
ν	=	kinematic viscosity
Φ	=	roll angle
Φ_0	=	initial roll angle
Ψ	=	yaw angle

Presented as Paper 1070 at the 45th AIAA Aerospace Sciences Meeting and Exhibit, Reno, NV, 8–11 January 2007; received 21 March 2007; revision received 19 February 2008; accepted for publication 29 February 2008.

*Research Scientist, Institute of Aerodynamics and Flow Technology, Lilienthalplatz 7; andreas.schuette@dlr.de (Corresponding Author).
†Research Scientist, Institute of Aerodynamics and Flow Technology, Lilienthalplatz 7.
‡Research Scientist, Institute of Flight Systems, Lilienthalplatz 7.
§Research Scientist, Institute of Aerodynamics and Flow Technology, Bunsenstrasse 10.
¶Research Scientist, Institute of Aeroelasticity, Bunsenstrasse 10.
**Research Scientist, Simulation and Software Technology, Linder Höhe.

I. Introduction

THE improvement of maneuverability and agility is a substantial requirement of modern fighter aircraft. Currently, roll rates of 200 deg /s and more can be achieved, especially if the design of the aircraft is inherently unstable. Most of today's, and probably future, manned or unmanned fighter aircraft will be delta-wing configurations. Already, at medium angles of attack, the flowfield of such configurations is dominated by vortices developed by flow separation at the wings and the fuselage. The delay in time of vortex position and condition to the on-flow conditions of the maneuvering aircraft can lead to significant phase shifts in the distribution of loads. In such a case, reliable results for the analysis of the flight properties can only be achieved by a combined nonlinear integration of the unsteady aerodynamics, the actual flight motion, and the elastic deformation of the aircraft structure. The dynamic aerodynamic effects on the vertical flow of pitching and rolling delta wings are discussed in several references. Among others, numerical investigations are given by Ericsson [1] and Arthur et al. [2], whereas experimental investigations are given by Chaderjian and Schiff [3,4], Hanff and Huang [5], and Hummel and Löser [6]. Within the Defense Advanced Research Projects Agency, several experimental investigations on aerodynamic structural-mechanics coupling effects are analyzed by wind-tunnel tests using an unmanned combat air vehicle model configuration, Kudva [7] and Sanders et al. [8].

The main objective of this paper is to focus on the necessity of developing a multidisciplinary engineering tool for predicting the unsteady critical states of complex maneuvering aircraft. Such a simulation environment has to bring together aerodynamics, aeroelasticity, and flight mechanics in a time-accurate simulation tool. To deliver such a tool, the DLR project SikMa (simulation of complex maneuvers) has been initiated to combine these three disciplines into one simulation environment [9,10]. For validating the numerical simulations, several wind-tunnel experiments in both the low-speed and transonic flow regime have been done within the SikMa project.

II. Numerical Approach

A. Computational Fluid Dynamics Solver TAU

The behavior of the fluid flow affecting the object of interest is simulated with the TAU code, a computational fluid dynamics (CFD) tool developed by the DLR Institute of Aerodynamics and Flow Technology [11–13]. The TAU code solves the compressible, three-dimensional, time-accurate Reynolds-averaged Navier–Stokes equations using a finite volume formulation. The code is based on a hybrid unstructured-grid approach, which makes use of the advantages that prismatic grids offer in the resolution of viscous shear layers near walls and the flexibility in grid generation offered by unstructured grids. The grids used for simulations in this paper were created with the hybrid grid generator Centaur, developed by Centaur Soft.[††] A dual-grid approach is used to make the flow solver independent from the cell types used in the initial grid. The unstructured-grid approach is chosen due to its flexibility in creating grids for complex configurations, for example, a full-configured fighter aircraft with control surfaces and armament. The TAU code consists of several different modules, including the following: 1) the preprocessor module, which uses the information from the initial grid to create a dual grid and the coarser grids for multigrid; 2) the solver module, which performs the flow calculations on the dual grid; 3) the adaptation module, which refines and derefines the grid to capture flow phenomena, like vortex structures and shear layers near viscous boundaries, among others; 4) the deformation module, which propagates the deformation of surface coordinates to the surrounding grid; and 5) the motion module, which is used to define the motion of the aircraft model and the relative motion of the control devices.

The main elements of the TAU code relevant for the SikMa project, in this case, the solver, preprocessor, adaptation, deformation, and chimera, have all been designed to work efficiently on massively parallel Linux clusters.

The solver module contains several upwind schemes, as well as a central scheme with artificial dissipation, which are used for the spatial discretization. For simulations of turbulent flows, the one-equation Spalart–Allmaras and several two-equation turbulence models are implemented. For steady computations, either an explicit Runge–Kutta-type time-stepping or an implicit lower upper-symmetric successive overrelaxation scheme [14] are used in combination with the multigrid technique. For time-accurate simulations, an implicit dual-time-stepping approach is used.

The TAU code can handle simulations containing multiple bodies in relative motion with one another, for example, motion of control surfaces with respect to the aircraft, by use of a hierarchical motion-node structure and the overlapping-grid chimera technique. The motion of each body can either be calculated internally by the TAU code, or supplied by an external program through a Python-implemented external interface.

1. TAU Code Module: Deformation

The deformation module accepts deformed surface coordinates either as absolute positions or as relative displacements from the previous surface grid. User-defined, rigid-body motions of the surface coordinates can also be used to specify the grid deformation. The input used for the cases presented in this paper is a deformed surface grid created by an external program. A deformed surface grid, containing points with new absolute positions, is written to a file, which the deformation module reads. The deformation of the surface grid is propagated through the primary grid, and a new primary grid is created. The preprocessor module uses this new primary grid to create the dual fine and coarse grids required by the solver module.

2. TAU Code Module: Adaptation

The adaptation module refines and derefines the primary grid using sensors and indicators that are based on flow-solution variables contained in the latest flowfield solution from the solver module. One of the sensors that have commonly been used in various flow simulations is the total pressure value; however, recently, new sensors have been implemented specifically to address vortex-dominated flow simulations. These new sensors are the λ_2 criteria and kinematic vortex-number N_k criteria, which take into account the rotation and rate of strain of the velocity gradient, and the normalized helicity H_n, which takes into account the angle between the translational and rotational velocity vectors. The new sensors are currently being evaluated as to their effectiveness in capturing the relevant flow phenomena in a vortex-dominated flowfield.

3. TAU Code Module: Motion

The motion module is not standalone executable but rather a library of functions that handle the rigid-body translational and rotational transformation matrix calculations for the TAU code. The module is built to take advantage of naturally occurring hierarchical motion structures, where, for example, flaps and slats inherit the motion of the wing to which they are attached.

4. TAU Code Extension: Chimera Technique

The chimera technique provides the capability to perform calculations with systems of overlapping grids. By allowing large relative body movement without the need for local remeshing or grid deformation, the technique is invaluable for the simulation of maneuvering combat aircraft, where large-amplitude control surface deflections and/or store release are a standard part of the simulation. An example is shown in Fig. 1 for the X-31 aircraft configuration. The current implementation can handle multibody simulations in which the overlapping-grid boundaries have been predefined; a version that allows "automatic hole cutting" is currently under development. The chimera search algorithm, which is based on a state-of-the-art alternating digital tree, is available for both sequential and massively parallel architectures. A more detailed description of the chimera approach is given by Madrane et al. [15].

B. Flight Mechanics

For the numerical simulation of the flight mechanics, the simulation environment SIMULA developed at the DLR Institute of Flight Systems is used [16]. SIMULA provides the three basic functionalities necessary for flight simulation and flight control purposes, trimming (the determination of the initial state and control values), linearization and stability analysis, and simulation (the numerical integration of the equations of motion).

Single and multibody flight-mechanics models, ranging from 1 to 6 degrees of freedom, are made available to the simulation by SIMULA. The amount of data that are exchanged between SIMULA and TAU is of a scale that can be easily communicated directly through a TCP/IP socket connection, which is offered by the simulation environment TENT.

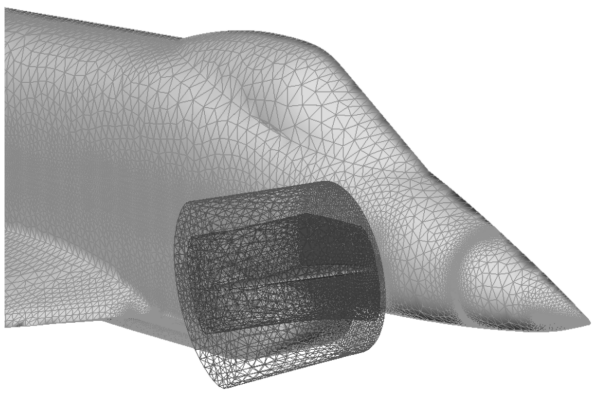

Fig. 1 Chimera mesh of the X-31 configuration.

[††]http://www.centaursoft.com

C. Structural Dynamics

Two different and independent approaches have been implemented for the coupled simulation in the time domain of aerodynamics, structural dynamics, and flight mechanics to better evaluate the more appropriate scheme for a given simulation complexity. Both approaches are based on a loose coupling scheme and use different software for spatial coupling, structural dynamics, and flight-mechanics simulation. The quality of the coupling is considered by verifying equilibrium of loads, energies, and work at each physical time step.

For the numerical verification of the coupled procedures, validated finite element (FE) models of the generic delta-wing configuration, which comprises the flexible delta wing mounted on the flexible wind-tunnel support, are available [17,18]. These models have been developed based on results of both ground vibration and static deformation tests.

1. *Modal Approach*

This approach is characterized by the use of the multibody system SIMPACK [19] to account for the elastic structure, as well as the flight mechanics, and its loose coupling to the computational fluid dynamics software TAU. It is called a modal approach because the structural elasticity is introduced from a modal solution of the discrete finite element model, thus receiving a linearly approximated and reduced elastic model that is based on a small number of modal degrees of freedom only. A reasonable number of structural modes have to be chosen to represent the appropriate dynamic behavior. The data exchanged between the multibody system (MBS) and CFD codes are spatially interpolated with the mesh coupling software MpCCI [20] and transferred through a TCP/IP internet socket.

The features of the modal approach comprising the topics of temporal and spatial coupling, structural and flight mechanical models, include the following [21]: 1) loose coupling for constant communication interval with CFD as master and MBS as slave process, the underlying temporal coupling scheme is the conventional serial staggered (CSS) algorithm [22]; 2) MBS time-integration method is an implicit second-order backward difference formulation (BDF2) algorithm; 3) use of conservative and nonconservative, element-based interpolation algorithms from the MpCCI coupling library to map the aerodynamic forces and the deformed mesh coordinates, respectively; 4) description of structural elasticity with a reduced, modal approximation computed from the FE model; and 5) consideration of all translatory and rotatory degrees of freedom in terms of flight mechanics from the MBS functionality.

2. *Discrete Approach*

The second aeroelastic method is the so-called discrete approach. Within this approach, the numerical integration of the structure mechanics equations of motion is performed with an implicit Newmark algorithm. The mass matrix and the stiffness matrix, which are obtained from a NASTRAN modal analysis, are reduced system matrices and include translatory degrees of freedom only. The reason for this lies in the fact that, in the spatial coupling process only, the translatory degrees of freedom (DOF) are involved.

The main characteristics of this fluid structure interaction in the time domain are as follows: 1) loose coupling of CFD and computational structure dynamics (CSD) through file input/output; 2) temporal coupling scheme based on the CSS [22,23] algorithm, modified with a predictor–corrector in each time step for the transformed structural forces; 3) use of an implicit Newmark algorithm for the time integration of the CSD equations of motion [24,25]; 4) use of different scattered data interpolation methods with and without compact support radius for spatial coupling [26]; and 5) the spatial coupling scheme is conservative with regards to the forces, moments, and work performed on both the aerodynamic and the structure dynamic model.

A detailed description of this approach can be found in [23]. The main difference between the modal and the discrete approach is that, in the discrete approach, all modes of the reduced finite element structure model and their dependency on each other are taken into account.

D. Integration Framework

For providing an applicable engineering tool, it is necessary to have an integration framework organizing the communication between the applications, the management of the simulation scenarios, the data transfer, and the capability to distribute the simulation on different computational platforms adapted for the different numerical codes. The integration framework TENT [27] provides a graphical user interface for controlling and monitoring coupled simulation workflows. The various codes used in the SikMa simulations will be made available in the TENT system, where a simulation workflow can be built by connecting icons representing each code using a graphical workflow editor. Java wrappers containing the basic control functionality for the TAU and SIMULA applications are already integrated in the TENT environment. The wrapper for the CSM code, as well as the extension of the functionality to handle the coupling between all three disciplines, is under development.

Whereas TENT provides the data transfer, the communication between the applications and the distribution of the applications on different computational platforms, the communication logic for the simulation workflow is contained within a coupling manager script. The coupling manager is a user-extensible script based on a Python and Java interface, where functionality to control the flow of the simulation has been implemented. In Fig. 2, the graphical user interface of the preprocessing tool SimBrowser is shown. The SimBrowser provides the capability to setup the model hierarchy, to define the motion of each element (e.g., flaps, rudder, etc.), and delivers the necessary motion- and hierarchy-input files for the flow solver.

III. Experimental Data

For the validation of the numerical simulation software, various wind-tunnel experiments, designed specifically for the SikMa project, are performed. Experimental data, both steady and unsteady, are available for a 65 deg swept delta-wing–fuselage configuration which has been tested in the DNW (German–Dutch wind tunnels) Transonic Wind Tunnel Göttingen (DNW-TWG). The model has movable trailing-edge flaps and can be used for both guided and free-to-roll maneuver simulations around its longitudinal axis. The model shown in Fig. 3 has a chord length of 482 mm and a span of 382 mm. For the verification of the aerodynamic-structure coupling, a static and dynamic system identification of the delta wing and the support within the wind tunnel is done. The system parameters are used to set up the FE model for the coupled simulation.

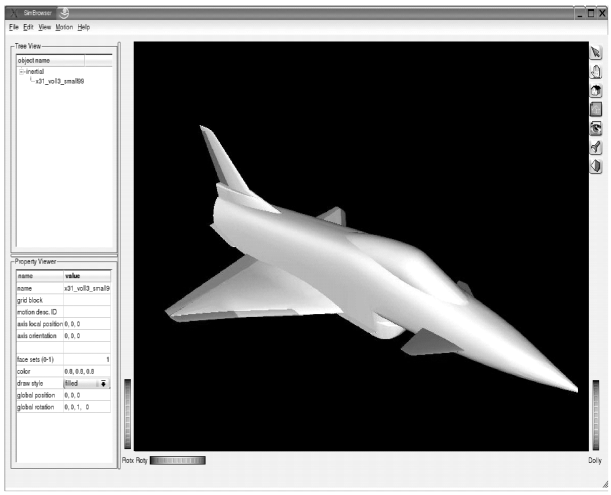

Fig. 2 Graphical user interface of the framework environment.

Fig. 3 Configuration of 65 deg swept delta-wing–fuselage model with remote-controlled trailing-edge flaps on the roll-rig device in the DNW-TWG Göttingen.

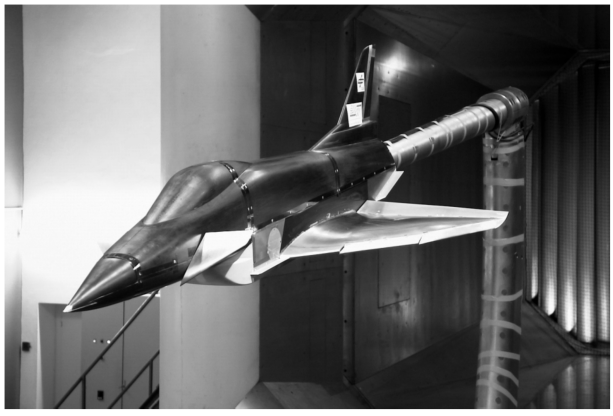

Fig. 4 X-31 remote-control model in the DNW-NWB Braunschweig.

The main experiments for the SikMa project are done in the DNW Low-Speed Wind Tunnel Braunschweig (DNW-NWB) [28]. To perform these experiments, a wind-tunnel model has been designed and built for the SikMa project. The model, shown in Fig. 4, is based on the X-31 experimental high-angle-of-attack aircraft configuration. The model is equipped with remote-controlled movable control devices driven by internal servoengines, as seen in Fig. 5. Measurement equipment is installed to determine the aerodynamic forces and moments on the model, as well as spanwise pressure distributions at locations of 60 and 70% chord length. The experiments include steady-state measurements using pressure sensitive paint (PSP), which provide detailed information on the surface pressure distribution for the whole wing. The experiments will culminate with maneuver simulations, where the movement of the aircraft and the control devices will be synchronized. For the maneuver experiments, the model will be mounted on the model positioning mechanism (MPM) of the DNW-NWB. Figure 6 shows the X-31 remote-control model mounted on the MPM system.

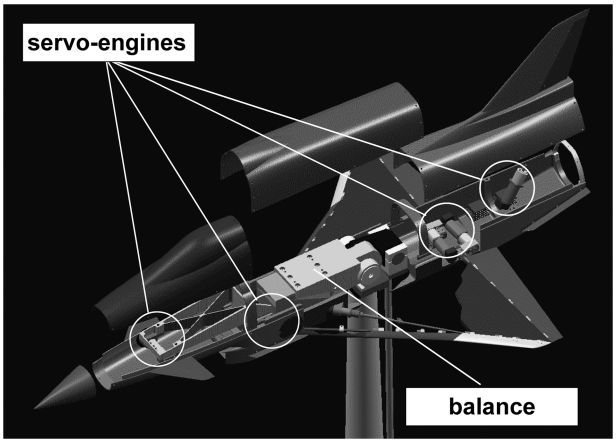

Fig. 5 Computer aided three-dimensional interactive application (CATIA) image of the X-31 wind-tunnel model.

Fig. 6 X-31 model on the model positioning mechanism in the DNW-NWB wind tunnel.

IV. Results

For the verification and validation of the simulation environment, the results of the numerical simulations are compared against data collected from various experimental simulations. For this purpose, a validation strategy is defined considering the model configurations and the test and validation scenarios. One of the model configurations is the delta-wing configuration described in Sec. III. The model is used to show the capability of the TAU code to predict the unsteady aerodynamic behavior of configurations with vortex-dominated flowfields. The final configuration is the X-31 model. Results for the delta-wing configuration will be shown for verification of the coupling procedures, after which, results for the validation of steady and unsteady simulations of the X-31 configuration will be presented.

A. Verification of the Coupling Procedure

In Fig. 7, a CFD–flight-mechanics coupled simulation of the delta wing with trailing-edge flaps is depicted. The initial attitudes are $\alpha = 17$ deg and $\Phi_0 = 0$ deg. The trailing-edge flaps are deflected by $\eta = \pm 5$ deg, once the model has been released. The computational grid has approximately $7 \cdot 10^6$ grid points, and the area close to the surface is resolved by 20 prismatic layers. The simulations for the delta wing, as well as for the X-31 configuration (discussed later), are done on 32 bit PC-cluster parallel on 32 and 48 processors,

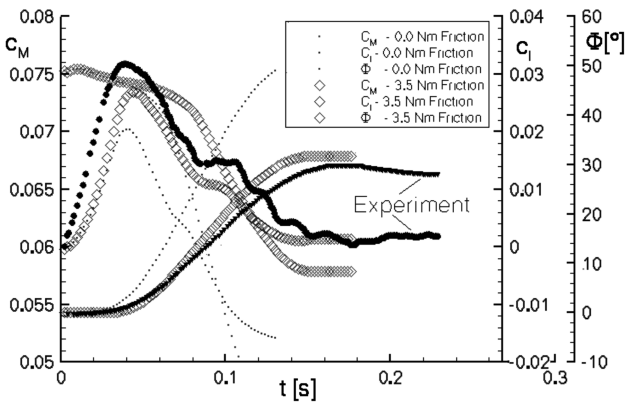

Fig. 7 One-DOF free-to-rollq maneuver of delta-wing–flap-configuration through trailing-edge flap deflection: $M = 0.5$, $Re = 3.8 \times 10^6$, $\Theta = 17$ deg, $\Phi_0 = 0$ deg, $\eta = \pm 5$ deg.

respectively. The physical time step size is $\Delta t = 0.001$ s, and 600 inner pseudo-time-steps are performed within each physical time step. The time for the chimera search within each physical time step can be neglected in comparison to the computational time for each physical time step. The turbulence model used for this simulation is the Wilcox k-ω turbulence model with the Kok- turbulent–nonturbulent (TNT)-rotational correction approach [29]. The Wilcox k-ω turbulence model with rotational correction is chosen based on experiences of other investigations simulating the flow around delta wings with sharp leading edges. Investigations by Arthur et al. [2] also give good results by using the Wilcox k-ω turbulence model. Two calculations are done using this configuration. The first calculation is done without taking into account the effects of mechanical friction, whereas the second calculation used a mechanical friction of 3.5 Nm. It was not possible to determine the friction of the model setup exactly by the experiment. From Arthur et al. [2], there are some approximations given between 2 and 4 Nm by using a comparable wind-tunnel model setup in the TWG. The characteristic movement of the model, as well as the roll-moment coefficient, is well predicted by the second calculation. By analyzing the roll-moment coefficient, we observe the following:

1) An asymmetric surface force-distribution develops due to the asymmetric trailing-edge flap deflection, which in turn leads to a rotational acceleration around the longitudinal axis of the model.

2) The maximum roll-moment coefficient is reached after a simulation time of 0.05 s, where the flaps are at $\eta = 2.5$ deg deflection. After this, the roll-moment coefficient decreases and reaches a temporary plateau at $t = 0.1$ s, at which time the flaps are fully deflected at $\eta = 5$ deg.

3) The model reaches a trim point at $\Phi = 31$ deg, where the combined roll moment is not large enough to overcome the aerodynamic damping due to the asymmetric loads on the wing together with the mechanical friction of the system.

The reason for the movement of the model is graphically explained in Fig. 8. At the start of the simulation, the wing is accelerated due to the asymmetric flap deflection (see Fig. 8a). The vortex on the luff side of the wing is strengthened with the increasing roll angle. The effective sweep angle on the luff side of the wing is decreasing, which in turn increases the normal component of the on-flow vector. This causes a stronger primary vortex on the luff side, which is located closer to the surface, thus leading to a higher local lift on the luff side. On the lee side, the opposite effect happens. The wing vortex gets weaker and the distance from the wing surface higher as the roll angle increases, which leads to a lower local lift on the lee side (see Fig. 8b). This effect causes the wing to decelerate, which in turn leads to the trim point at $\Phi = 31$ deg (Figs. 8c and 8d).

This example shows the capability of CFD–flight-mechanics coupling by means of a delta wing with trailing-edge flaps. The main aerodynamic effects are qualitatively well predicted, but, to predict the quantitative aerodynamic values obtained experimentally, it is necessary to have the same starting conditions and environment

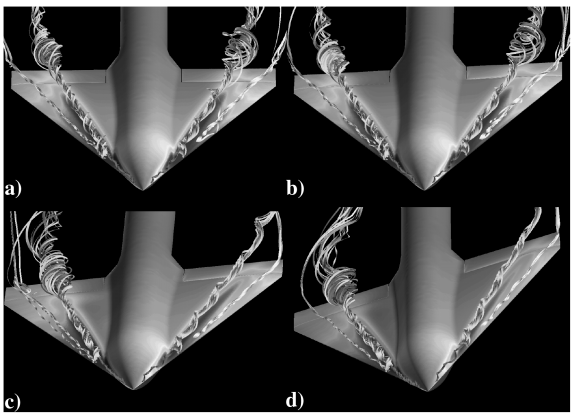

Fig. 8 One-DOF free-to-roll maneuver of delta-wing–flap-configuration through trailing-edge flap deflection. Flow topology at four different stages: $M = 0.5$, $Re = 3.8 \times 10^6$, $\Theta = 17$ deg, $\Phi_0 = 0$ deg, $\eta = \pm 5$ deg.

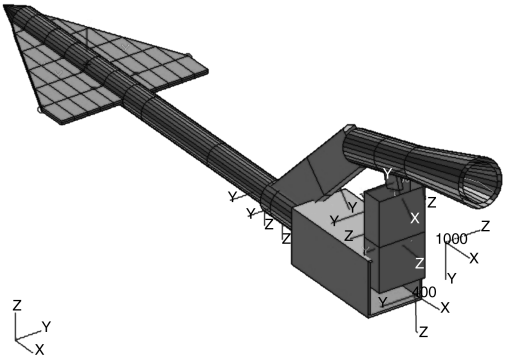

Fig. 9 FE model of the wind-tunnel setup comprising the generic delta wing and the model support.

parameters that were in effect during the experimental maneuver scenario.

The capability to predict the elastic deformations accurately is demonstrated for the delta-wing configuration during a guided roll maneuver for both the discrete and modal approach. The delta wing and the rear-sting support are considered to be elastically deformable within the coupled simulation between the TAU code and the structural dynamics tools. For the coupled simulation, the finite element model [18] takes into account both the delta-wing configuration as well as the flexible support, as seen in Fig. 9. The FE model is validated based on results of both ground vibration and static deformation tests. The aerodynamic calculations are performed in Euler mode using a coarse mesh topology for the reduction of computation time on the CFD side. This procedure is sufficient to verify the general capabilities of the two developed approaches.

The guided maneuver is a constant rotation at 5 Hz of the wing body around its own longitudinal axis. The on-flow velocity is at a Mach number of 0.5 and the pitch angle, that is, angle of attack for zero roll angle, is 6 deg. The corresponding history of the model deflection is depicted in Fig. 10 for the sting support at the trailing-edge position of the delta wing. It can be seen that the sting is undergoing an elliptical-like motion during the guided maneuver. The light gray curve in Fig. 10 shows the sting movement from the experiment which is integrated from the measured accelerations. A comparison of the numerical results computed from the discrete and modal approach shows a good agreement of the predicted motion at the sting position with the measured data. Because of the elastic deformation, which is rather dominated by the model sting bending than the deflection of the generic delta wing, the effective angle of

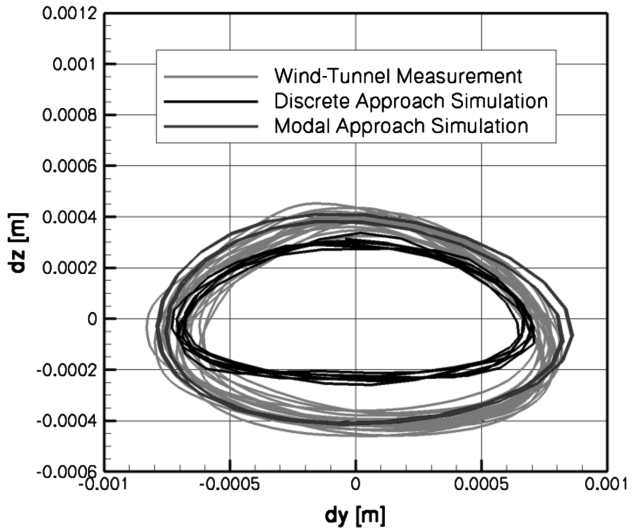

Fig. 10 History of the delta-wing sting deflection during elastic-body motion in comparison to experiment. Time-accurate coupled CFD (Euler)-CSM simulation.

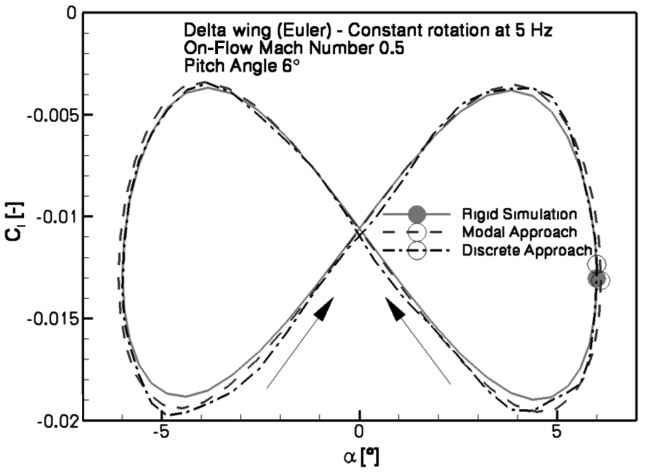

Fig. 11 Comparison of rolling moment between rigid- and elastic-body motion of delta wing during constant rotational movement. Time-accurate coupled CFD (Euler)-CSM simulation.

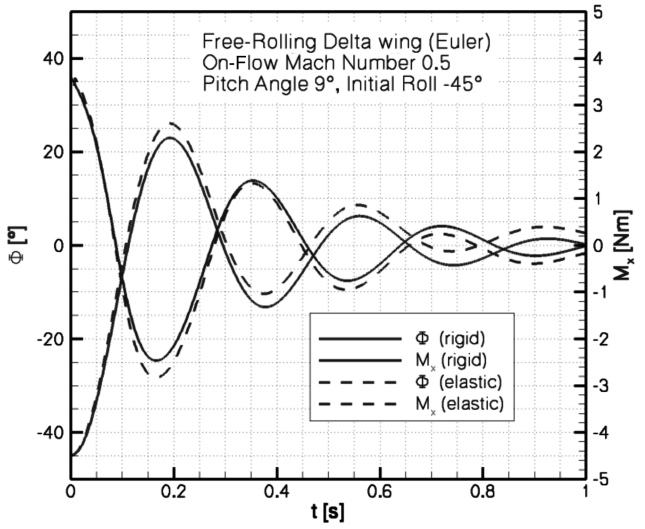

Fig. 12 Comparison of rolling moment and roll angle between rigid and elastic-body motion of delta wing during free-to-roll motion. Time-accurate coupled CFD (Euler)-CSM-FM (flight mechanic) simulation.

attack has increased for a given roll angle, leading in turn to higher values for the rolling moment coefficient, as presented in Fig. 11.

The time-history results for the rigid and the coupled elastic simulation, performed with the modal approach, for the free-to-roll wind-tunnel maneuver are compared in Fig. 12 for roll angle Φ and rolling moment M_x, respectively. The on-flow Mach number is at $M = 0.5$, the pitch angle is 9 deg, and the initial roll angle is at 45 deg. As described before, the maneuver is initiated by the unsymmetrical load distribution over the wing surface due to the initial roll angle. Furthermore, similar elastic effects occur as already found with the simulation of the guided maneuver. The elastic deformations of the support in the lateral y and vertical z direction lead to locally increased angles of attack and thus to larger aerodynamic loads, resulting in a changed rolling moment around the body-fixed x axis of the delta wing, according to Figs. 12 and 13. In contrast to the rigid result, the elastic simulation shows a roll angle with an offset of approximately 2.5 deg. The reason is found in the pitch- and yawlike contributions from the elastic deflection of the axis of rotation, which is considered for the computation of the aerodynamic loads. In the remainder of the paper, further RANS calculations comparisons with experimental data will be done.

In Fig. 14, the delta-wing model is used to show the trimming capability of the CFD–flight-mechanics coupling procedure. The convergence of the trim algorithm is good. There are only a few time

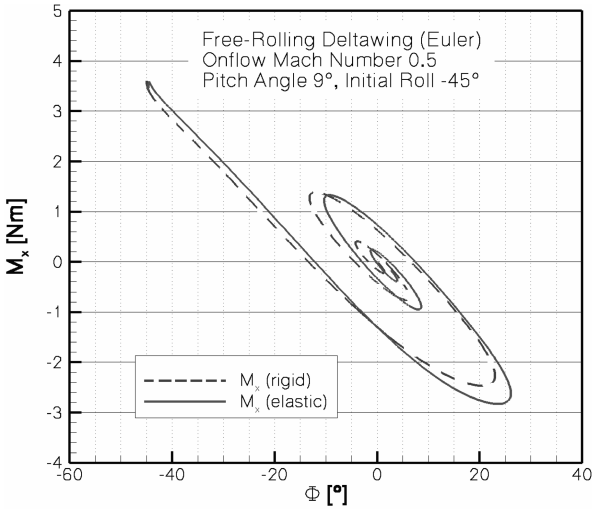

Fig. 13 Comparison of rolling moment between rigid- and elastic-body motion of delta wing during free-to-roll motion. Time-accurate coupled CFD (Euler)-CSM-FM.

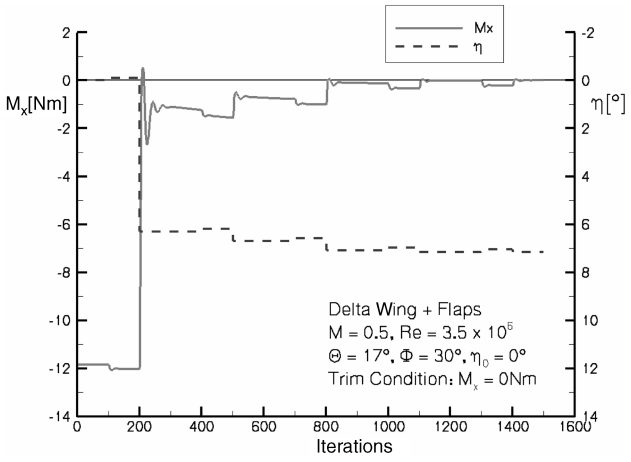

Fig. 14 Characteristics of rolling moment M_x and flap deflection angle η during a trimming scenario.

steps necessary to get a converged trim point. The convergence of the TAU code within every trim loop is usual for this type of model simulation. The initial conditions are shown in Fig. 15: $M = 0.5$, $\Theta = 17$ deg, $\Phi = 30$ deg, and $\eta_0 = 0$ deg. The trimming algorithm uses a gradient-based approach to determine the direction and magnitude of the flap deflection. The desired trimming condition is a rotational acceleration magnitude of zero around the longitudinal

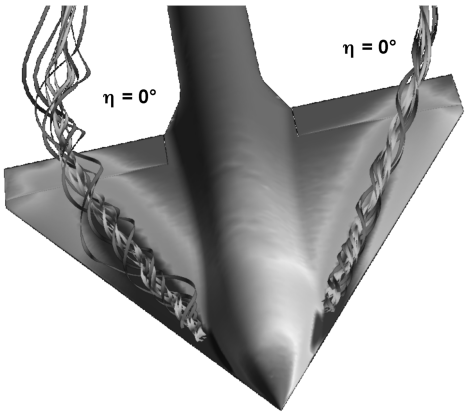

Fig. 15 Initial state of trimming scenario. Surface pressure distribution and streamlines. $M = 0.5$, $\Theta = 17$ deg, $\Phi = 30$ deg, $\eta_0 = 0$ deg.

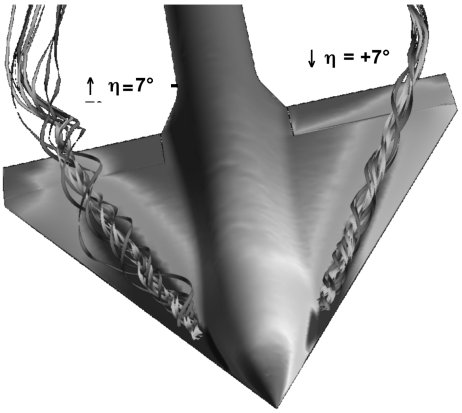

Fig. 16 Final state of trimming scenario. Surface pressure distribution and streamlines. $M = 0.5$, $\Theta = 17\,\text{deg}$, $\Phi = 30\,\text{deg}$, $\eta = \pm 7\,\text{deg}$.

axis of the delta wing. In Fig. 15, the surface distribution and flow topology of the primary vortices are depicted for the nontrimmed conditions. Because of the asymmetric flow conditions, the luff vortex on the left-hand side is stronger and closer to the surface of the wing. This causes a locally higher lift on the luff side in comparison to the lee side, where the vortex is weaker and farther away from the surface. This causes a negative damping rolling moment which has to be compensated by flap deflection. In Fig. 16, the surface distribution and flow topology of the primary vortices are shown for the trimmed condition, where the flaps have been deflected by $\eta = \pm 7$ deg. It is seen that the vortex structure is not influenced by the flap deflection. The only significant difference is a higher suction peak over the flap on the lee side of the wing due to the upward deflection of the flap.

B. Validation for the X-31 Configuration

Having presented the principal capabilities of the coupling procedures by means of the simple delta-wing model, the next step is to determine the capability to accurately capture the steady and unsteady aerodynamics of the more complex X-31 configuration by comparing the numerical results with experimental data.

In Fig. 17, the topology of the computational model for the simulation of the X-31 configuration is shown. All control devices are taken into account and two different setups are simulated. The first setup is simulated with a rear-sting support. For the second, a belly sting support is mounted on the lower side of the model for the unsteady calculations as it is configured in the experiments. In Fig. 18, the hybrid mesh topology is depicted. A prerefined mesh is used for both steady and unsteady simulations. To cover a certain range of pitching and yawing angle, the prerefinement is adapted to the areas where the vortices are assumed during the simulation. The steady-state results are simulated with no sting, whereas the unsteady simulations are simulated with the belly sting support taken into account, as was the case in the experiments. The effect of the support is discussed later.

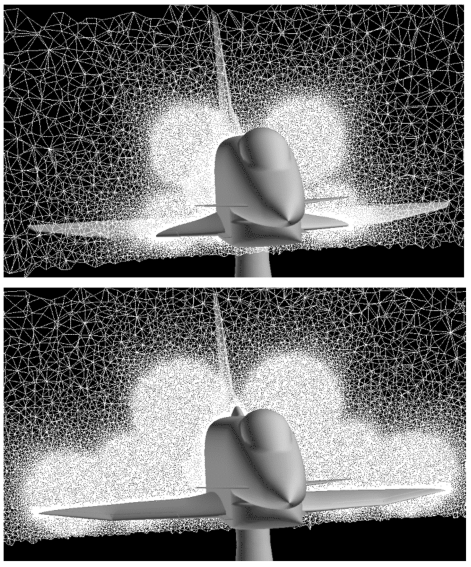

Fig. 18 Slices through prerefined unstructured hybrid mesh of the X-31 configuration.

Figure 19 shows the numerically simulated 3-D flowfield over the X-31 configuration, and gives a good indication of the complexity of the vortex flow topology over the wing and fuselage. For this simulation, the clean-wing configuration is used to evaluate the capability to capture the complex flowfield over the wing. Comparisons with experimental data show good agreement regarding the vortex topology. In Fig. 20a, an oil flow picture of the X-31 clean wing from low-speed experiments is shown. The angle of attack is $\alpha = 18\,\text{deg}$ at a Reynolds number of 10^6. The attachment line of the strake vortex and the main wing vortex, as well as the separation line of the main wing vortex near the leading edge, is emphasized. In Fig. 20b, the corresponding CFD calculation is depicted. It is seen that the flow topology from the calculation fits quite well with the experiment.

Further calculations were done taking all control devices into account. This means that all gaps between the trailing- and leading-edge flaps and the wing are represented by the computational model. In these simulations, a computational grid with approximately 15×10^6 grid points is used. The boundary-layer region is resolved by 20 prismatic layers. For the unsteady simulations, a physical time step of $\Delta t = 0.02$ is used and 1000 inner pseudo-time-steps are necessary within each physical time step. The maneuver simulations are resolved with 50 time steps per period. In comparison to the delta wing with sharp leading edges, the X-31 is a configuration with rounded leading edges. First investigations using the Wilcox k-ω

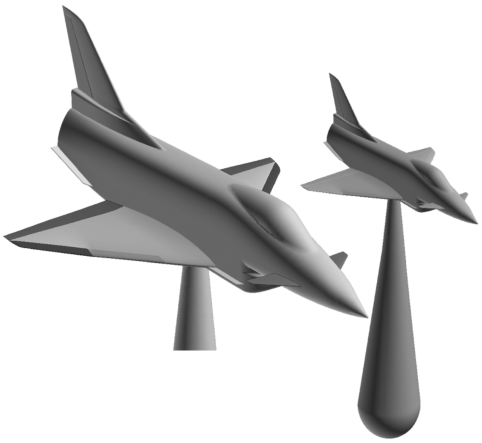

Fig. 17 X-31 model topology for the computational simulation.

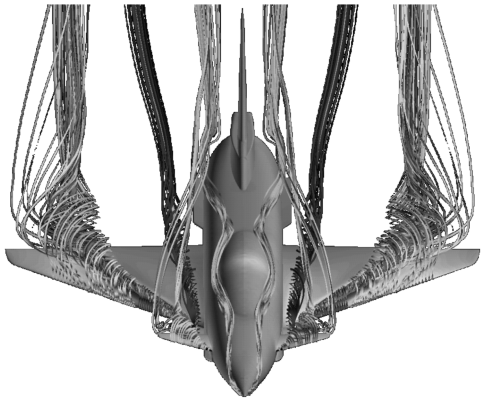

Fig. 19 Three-dimensional flowfield over the X-31 configuration at 18 deg angle of attack.

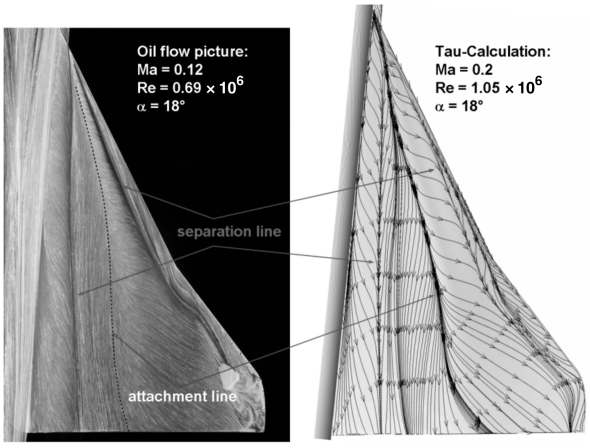

a) b)

Fig. 20 a) Oil flow visualization of the X-31 clean wing at $\alpha = 18$ deg. b) TAU calculation. Visualization of surface streamlines at $\alpha = 18$ deg.

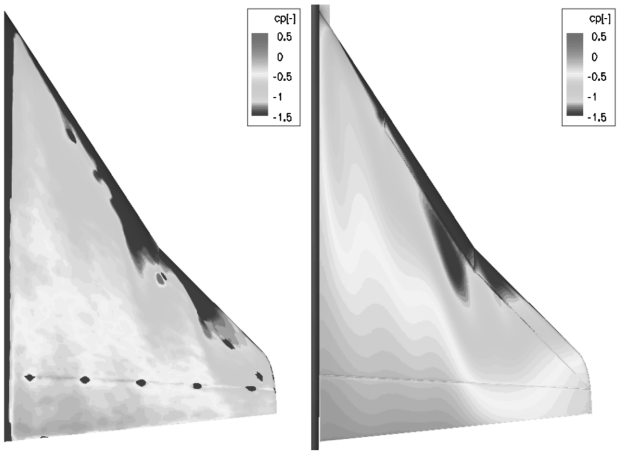

a) b)

Fig. 21 Pressure distribution over the X-31 wing: a) steady PSP measurement, b) steady TAU RANS calculation.

turbulence model do not show satisfactory results for configurations with rounded leading edges. Hence, for the X-31 simulations, the one-equation Spalart–Allmaras turbulence model is used. Investigations by Fritz [30] have also shown good results for configurations with blunt leading edges comparable to the X-31 by using the Spalart–Allmaras turbulence model. In Fig. 21a, the PSP result at $\alpha = 16$ deg at a Reynolds number of 2.07×10^6 is shown. Comparing the pressure distribution from the PSP measurement with the CFD calculation in Fig. 21b, it is seen that the main footprints of the vortices, as well as the location, are captured by the CFD numerics. The main difference with respect to the clean-wing configuration discussed in Figs. 19 and 20 is the separated vortex shear layer, which occurs due to the gaps between the leading-edge control devices. This leads to a more complex vortex topology with three vortices. The first vortex comes from the inner wing, and the second and third from the inner and outer flap, respectively. The suction strength of the vortex at the inner leading-edge flap is predicted to be stronger, and the outer vortex starting at the kink of the wing is predicted to be weaker than in the experiment.

In Fig. 22, the lift and pitching-moment coefficient over the angle of attack are shown. For all calculations at 10, 12, 14, and 16 deg angle of attack, a higher front-loading pitching moment is predicted by the numerics, whereas the overall lift is fairly well predicted by the CFD calculation. The reason for this can be identified by looking at the pressure distribution on the canard and the two stages at 60 and 70% cord length in Figs. 23–26. For 12 deg angle of attack and higher, the suction peak over the canard is predicted too low. This

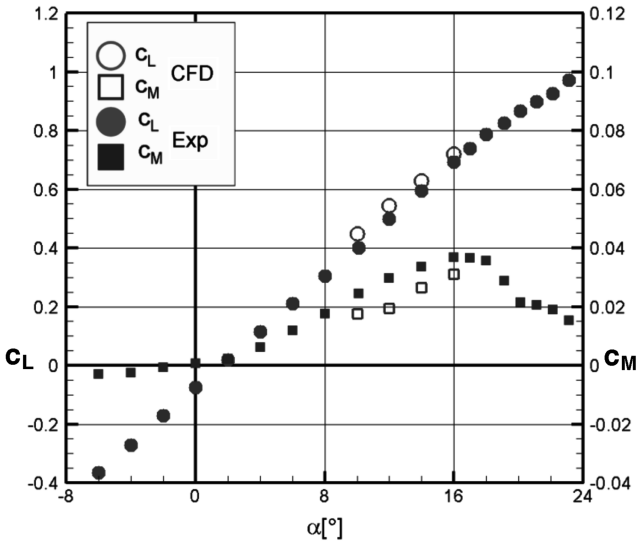

Fig. 22 Lift and pitching-moment coefficient over angle of attack. Comparison of TAU calculations with experimental data.

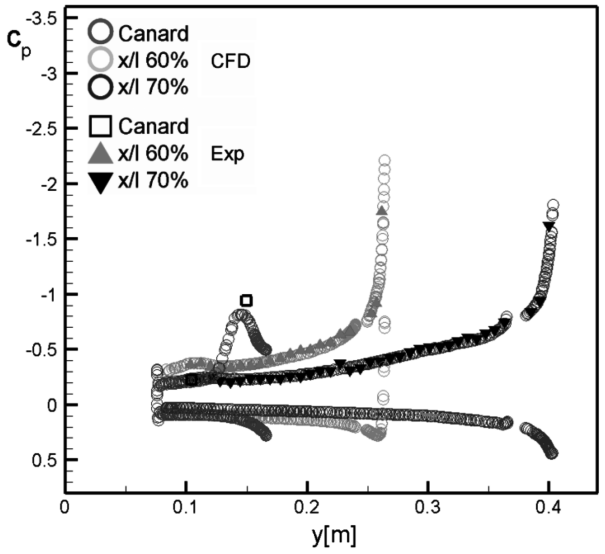

Fig. 23 Comparison of the pressure distribution at an angle of attack of $\alpha = 10$ deg.

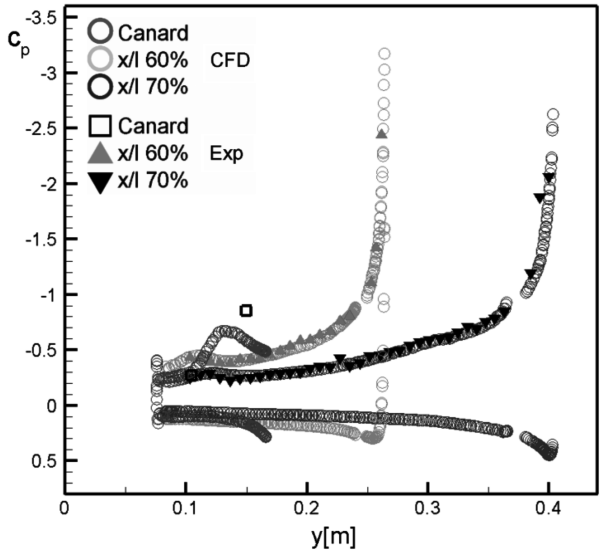

Fig. 24 Comparison of the pressure distribution at an angle of attack of $\alpha = 12$ deg.

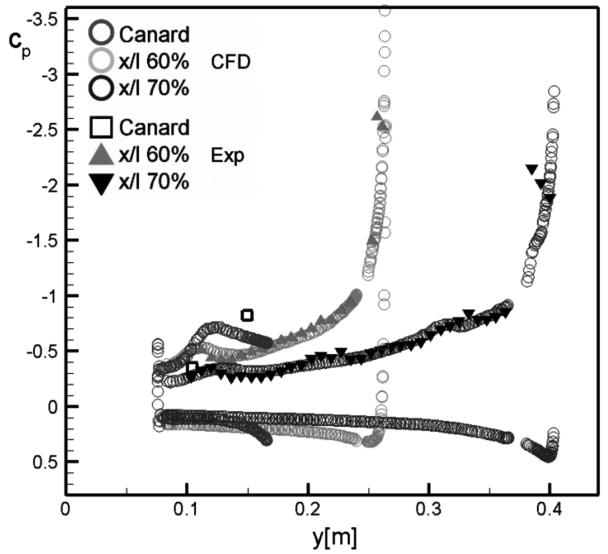

Fig. 25 Comparison of the pressure distribution at an angle of attack of $\alpha = 12$ deg.

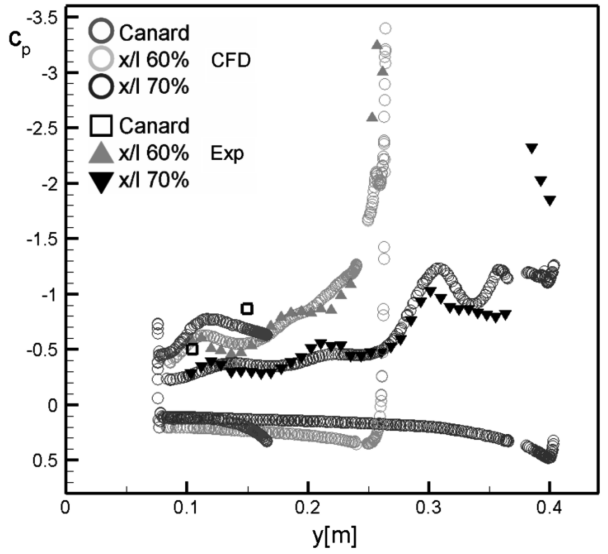

Fig. 26 Comparison of the pressure distribution at an angle of attack of $\alpha = 10$ deg.

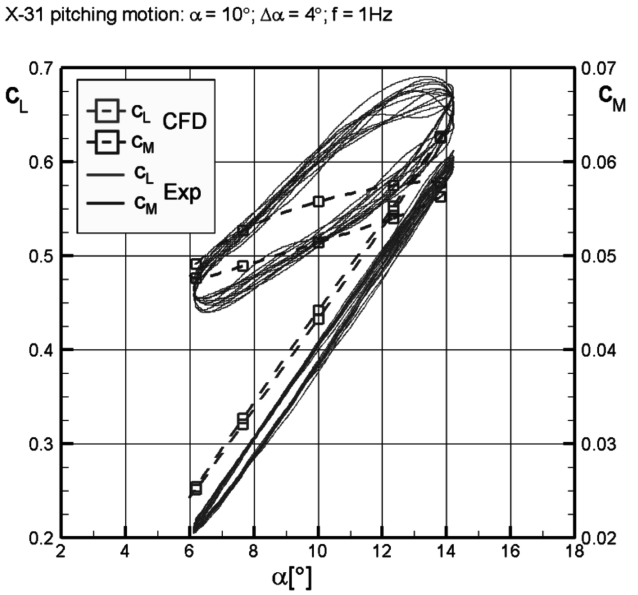

Fig. 27 Guided pitching motion of the X-31 configuration. Comparison of TAU calculations with experimental data.

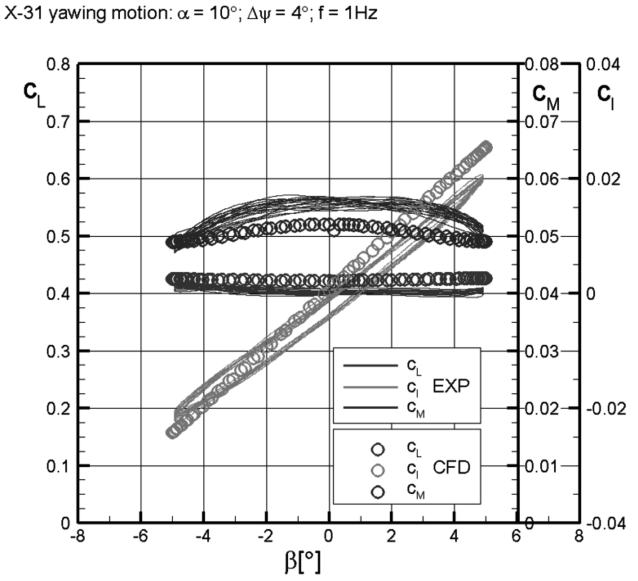

Fig. 28 Guided yawing motion of the X-31 configuration. Comparison of TAU calculations with experimental data.

causes a lower contribution for a rear-loading pitching moment of the canard. Regarding the pressure distribution on the wing, it is seen that overall pressure distribution is well predicted by CFD. However, the formation of the vortex at the outer leading-edge flap occurs at a somewhat higher angle of attack than in the experiment. The difference between experiment and numerical simulation is easily observable in Fig. 27 at 70% cord length, where no outer vortex is shown by the numerics, whereas, in the experiment, a high suction vortex peak is measured.

Figure 28 shows the result of a guided yawing motion maneuver. The initial pitching angle is 10 deg and the yaw amplitude is $\Delta\beta = 5$ deg. The maneuver is done with a frequency of 1 Hz. In this scenario, the model is mounted on the belly sting support described earlier. The overall aerodynamic behavior is captured by the numerical simulation, although the pitching moment is under-predicted. The gradient of the rolling moment is predicted to be higher than in the experiment, and the hysteresis shown in the experiment is predicted to be lower by the calculation. Comparing the initial pitching moment in Fig. 28 at 10 deg to the steady-state results in Fig. 22, it is seen that the pitching moment in the case of the belly sting is more than double that without sting. The reason for this is that the belly sting is shifting the local angle of attack of the inner wing to higher values. This causes a higher suction and a corresponding higher front loading on the wing. Furthermore, the induced angle of attack of the canard is rising, which leads to a higher lift on the canard and higher rear-loading pitching moment.

Figure 27 shows the result of a guided pitching motion maneuver. The initial pitching angle in this case is 10 deg with an amplitude of $\Delta\alpha = 4$ deg. The maneuver is again done with a frequency of 1 Hz. As in the case of yawing motion, the lift is predicted higher than in the experiment. The gradient is predicted correctly. Unfortunately, the characteristic of the dynamic pitching moment is not given precisely by the numerical simulation. The reason is the same as described in the steady-state case before. Figures 29 and 30 show the flow topology at the lower and upper points of the dynamic loop. In Fig. 29, the flow is attached over the wing at $\alpha = 6$ deg, and even the flow around the canard is attached. Only a small vortex is generated from the strake in front of the inner wing. In Fig. 30, at $\alpha = 14$ deg, the flow topology has changed overall. Over the wing, a vortex

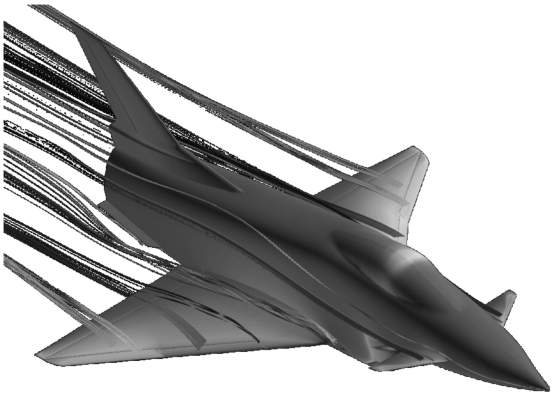

Fig. 29 Flow topology during pitching maneuver at $\alpha = 6\,\mathrm{deg}$. Streamlines and surface pressure distribution.

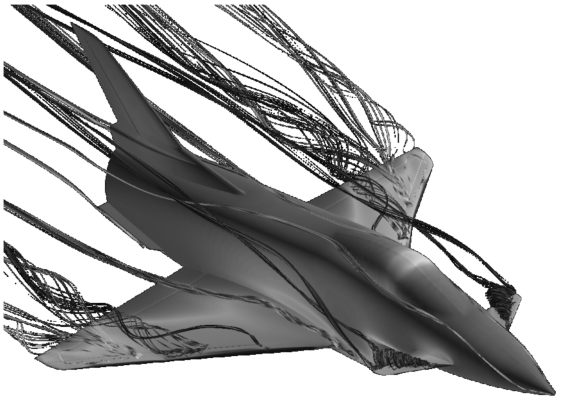

Fig. 30 Flow topology during pitching maneuver at $\alpha = 14\,\mathrm{deg}$. Streamlines and surface pressure distribution.

structure of four vortices starting from the wing strake, at the inner wing and from the inner and outer leading-edge flap, has developed. The inner wing vortex and the vortex from the inner leading-edge flap unify at approximately 70% cord length. Over the canard, a strong vortex is generated that does not interact with the wing vortices. The small strakes at the nose of the fuselage prevent the appearance of rolling instabilities caused by time-dependant flow separations.

Having provided initial validation results showing the capability to predict the overall flow topology around the X-31 configuration, the scenarios are extended to CFD–flight-mechanics coupled simulations. The initial stage is a trimming simulation for the complex X-31 configuration. The results obtained at the end of the trimming simulation are then the initial state for further free-flight maneuver simulations.

Figure 31 shows the convergence of the pitching moment, along with the corresponding flap deflection, of a trimming simulation for the X-31 configuration. As discussed before in the delta-wing case, the convergence of the trim algorithm is good. There are more iterations necessary within each TAU code loop in comparison with the delta-wing case, due to the higher complexity of the model configuration. The initial flight state is as follows: weight of 30 kg, thrust of 50 N, altitude of 10,000 ft, Mach number of 0.3, angle of attack of 5 deg, pitch angle of 5 deg, and trailing-edge flap deflection of -1.72 deg. The trimming requirements are an angle of attack of 5 deg, with longitudinal acceleration (translational and rotational) of zero. The trim module determines a new flight state dependent on the gradient calculations for the translational velocity components u and w, the pitch angle Θ, and the flap deflection angle η. The result of the trimming simulation is the following flight state: Mach number of 0.29, angle of attack of 5 deg, pitch angle of -1.55 deg, trailing-edge flap deflection of -0.18 deg, and a flight-path angle of -6.55 deg.

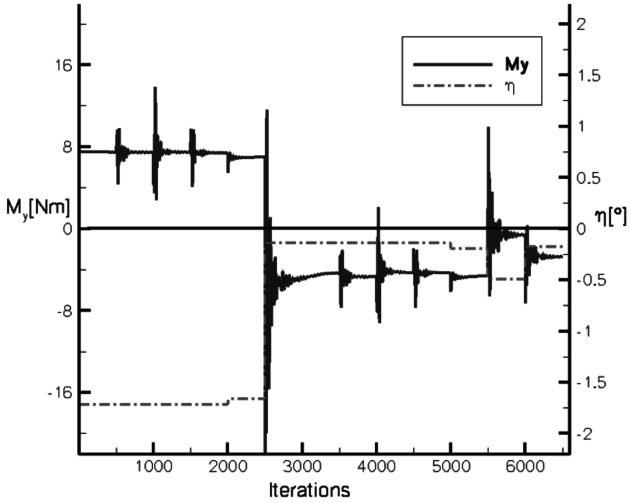

Fig. 31 Convergence of the pitching moment during trimming simulation and the corresponding trailing-edge flap deflection.

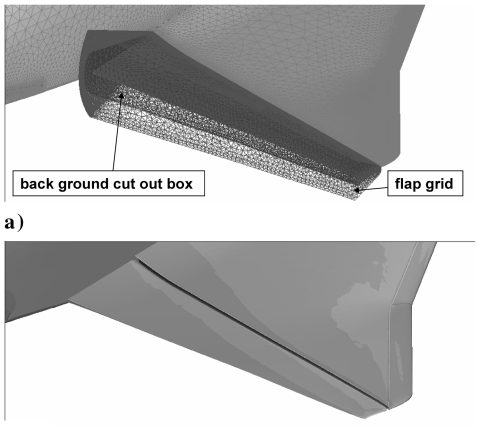

Fig. 32 Overlapping chimera grids at the a) right trailing-edge flap, and b) pressure-coefficient distribution at the trimmed flight conditions.

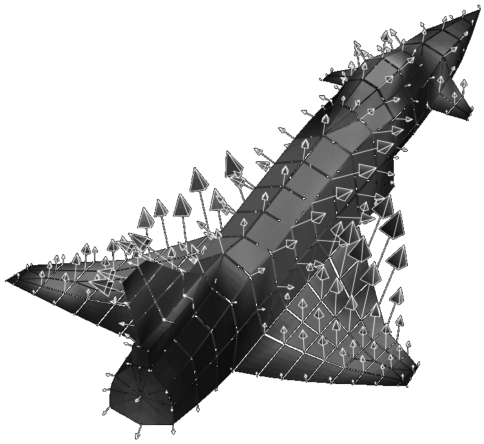

Fig. 33 Structural deformation of the FE model and corresponding forces on the aircraft. One time step within an unsteady maneuver simulation.

Figure 32 shows the overlapping chimera grids around the right trailing-edge flap and the surface pressure coefficient for the same section at the trimmed flight-state conditions.

In the final application, the simulation of a free-to-roll maneuver of a generic aeroelastic model of the X-31 wind-tunnel model was

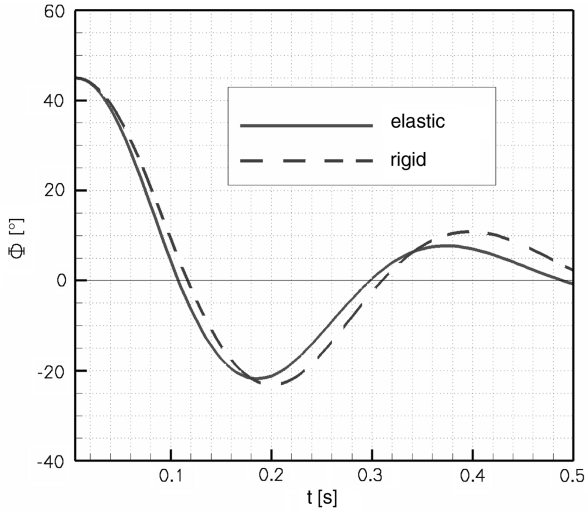

Fig. 34 Corresponding rigid and elastic position of the X-31 configuration during a free-to-roll maneuver around the longitudinal axis.

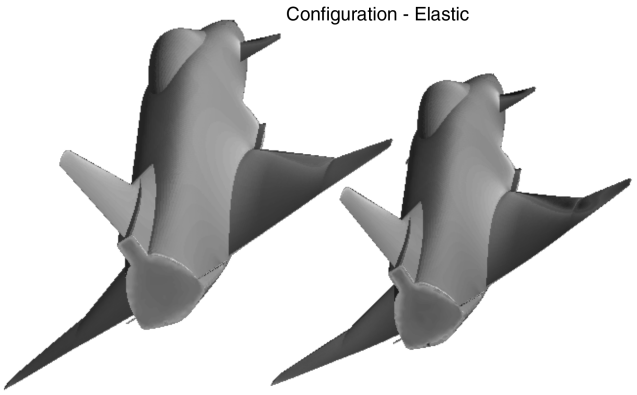

a) b)

Fig. 35 Pressure distribution for a) rigid and b) elastic CFD model of the X-31 configuration. Rolling angle at approximately $\Phi = -20\,\mathrm{deg}$ (at $t = 0.2$ s in Fig. 34).

performed. The objective of this test case is to show the capability of the implemented fluid-structure–flight mechanic simulation to handle complex configurations. The results for this maneuver are shown in Figs. 33–36. The simulation is a free-to-roll maneuver of the elastic X-31 configuration around the longitudinal axis. The full aircraft configuration with fuselage, wings, and control surfaces is contained in the structural model. The structure of the X-31 model is generic and has been designed such that the deformations during the flow conditions in the wind tunnel are clearly visible. The finite element model has 273 nodes with 819 discrete translational degrees of freedom and is depicted in Fig. 33. Euler computations have been performed on a mesh with 19.4 million tetrahedrons, 3.44 million nodes, and 261,792 nodes on the surface. To simulate the free-to-roll maneuver around the longitudinal axis, a simplified 1 degree-of-freedom flight mechanic model was used. This means that the acceleration of the model is dependent only on the aerodynamic rolling moment M_x and the moment of inertia around the x axis of the finite element model.

The simulated maneuver starts from a roll angle of 45 deg and a pitch angle of 15 deg. A converged, steady-state solution of the aerodynamic forces and moments was obtained for the undeformed mesh. During the maneuver, unsteady nonsymmetric loads on the aircraft lead to nonsymmetric deformation of the structure. The elastic model is depicted in Fig. 33. Shown are the deflected finite element model and the corresponding transformed aerodynamic forces. In Fig. 34, the comparison of the rolling angle during a real time of 0.5 s between the rigid and the elastic model is shown. It is seen that the rolling angle for the simulation with the elastic model converged quicker to a rolling angle of 0 deg. The reason for this is the higher aerodynamic moment M_x due to the elastic behavior of the finite element model. The deflection of the elastic model due to the aerodynamic forces induces a higher angle of attack and leads to a higher rolling moment. Because of the 1 degree-of-freedom flight mechanic model, the acceleration of the rolling angle is only dependent on the aerodynamic moment M_x, which is dependent on the elastic deformation. Because of the elastic behavior of the model, the rotational acceleration is higher than for the rigid model, which leads to a higher rolling frequency. This, in turn, leads to a higher aerodynamic damping of the system, which has an effect of bringing the system to a trimmed position within a shorter period of time than is observed with the rigid model. For this simulation, the comparison of the corresponding pressure distributions for the rigid and the elastic CFD model are shown in Fig. 35. The pressure distributions differ strongly from each other between the rigid and the elastic models. Because the loads on the configuration are asymmetric during the maneuver, the displacements due to the transformed structural loads on the left- and right-hand side differ from each other. In Fig. 36, the difference of the aerodynamic surface between the rigid and the full elastic model during the maneuver simulation is shown. The maximum displacement at the wing tip is approximately 3.8 cm for a half-span of the model of 50 cm. This simulation has shown the capability of the implemented coupling algorithms and data-exchange logic to simulate a maneuver which relies on high-fidelity aerodynamics, finite element modeling, and flight mechanics. With further investigations, RANS calculations will be done taking the deformation of the control devices into account.

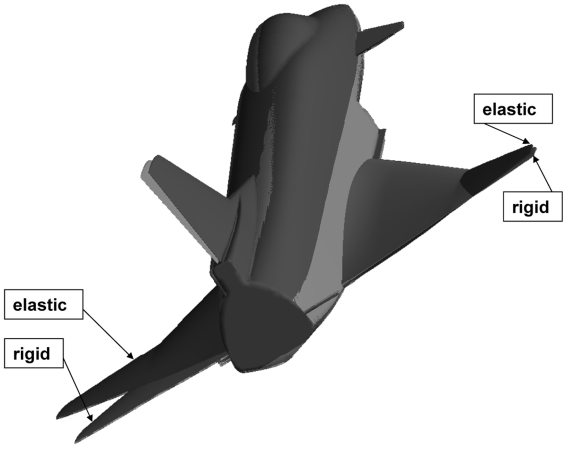

Fig. 36 Deformation of elastic CFD surface compared to rigid CFD surface during the free-to-roll maneuver.

V. Conclusions

In this paper, the activities and recent results of the DLR project SikMa were presented. In SikMa, a simulation tool should be developed that is capable of simulating a maneuvering elastic aircraft with all its movable control devices. The simulation tool combines time-accurate aerodynamic, aeroelastic, and flight-mechanics calculations to achieve this objective. Preliminary verification of the functionality of the simulation tool has been shown by simulating a sharp leading-edge delta wing during free-to-roll maneuvers due to flap deflections. First perspectives were presented regarding the time-accurate coupling between the TAU code, CSM code, and flight mechanics. Initial results of the steady and unsteady flowfield around the X-31 configuration were presented. The trimming algorithm was demonstrated using the X-31 configuration. Finally, a free-to-roll maneuver was presented using the X-31 configuration in a time-accurate coupling of CFD, CSM, and flight mechanics. Regarding the steady and unsteady RANS results, there are differences, especially looking at the pitching moment at higher angles of attack. Therefore, additional simulations might be necessary to validate the

TAU code for the X-31 configuration. This implies, as well, the use of different physical models like detached eddy simulations, which will probably capture the unsteady vertical flow physics better. Therefore, all control devices will be taken into account within a maneuver simulation as it was performed in the experiments.

Acknowledgments

The authors would like to thank Martin Rein, Gebhard Höhler, Peter Klemens, and Hartmut Haselmeyer for providing the wind-tunnel data and for their engagement managing the experimental simulation tasks at DLR Göttingen within the project Simulation of Complex Maneuvers.

References

[1] Ericsson, L. E., "Dynamic Stall of Pitching Airfoils and Delta Wings, Similarities and Differences," *Journal of Aircraft*, Vol. 36, No. 3, 1999, pp. 603–605. doi:10.2514/2.2477

[2] Arthur, M. T., Brandsma, F., Ceresola, N., and Kordulla, W., "Time Accurate Euler Calculations of Vortical Flow on a Delta-Wing in Pitching Motion," AIAA Paper 1999-3110, 1999.

[3] Chaderjian, N. M., "Navier–Stokes Prediction of Large-Amplitude Delta-Wing Roll Oscillations," *Journal of Aircraft*, Vol. 31, No. 6, 1994, pp. 1333–1340. doi:10.2514/3.46656

[4] Chaderjian, N. M., and Schiff, L. B., "Numerical Simulation of Forced and Free-to-Roll Delta-Wing Motions," *Journal of Aircraft*, Vol. 33, No. 1, 1996, pp. 93–99. doi:10.2514/3.46908

[5] Hanff, E. S., and Huang, X. Z., "Roll-Induced Cross-Loads on a Delta Wing at High Incidence," AIAA Paper 91-3223, Sept. 1991.

[6] Hummel, D., and Löser, T., "Low Speed Wind Tunnel Experiments on a Delta Wing Oscillating in Pitch," *21st Congress of the International Council of the Aeronautical Sciences*, International Council of the Aeronautical Sciences, 98–3.9.3, 1998.

[7] Kudva, J. N., "Overview of the DARPA Smart Wing Project," *Journal of Intelligent Material Systems and Structures*, Vol. 15, No. 4, 2004, pp. 261–267. doi:10.1177/1045389X04042796

[8] Sanders, B., Martin, C. A., and Cowan, D. L., "Aerodynamic and Aeroelastic Characteristics of the DARPA Smart Wing Phase II Wind Tunnel Model," *SPIE Symposium on Smart Structures and Materials*, Society of Photo-Optical Instrumentation Engineers Paper No. 4332-49, 2001.

[9] Schütte, A., Einarsson, G., Schöning, B., Madrane, A., Mönnich, W., and Krüger, W., "Numerical Simulation of Manoeuvring Aircraft by Aerodynamic and Flight Mechanic Coupling," *Proceedings of the Research and Technology Organization (RTO) Symposium on Reduction of Military Vehicle Acquisition Time and Cost Through Advanced Modelling and Virtual Production Simulation*, Defence Technical Information Center, Fort Belvoir, VA, 2003, p. 46-1—46-12.

[10] Schütte, A., Einarsson, G., Schöning, B., Raichle, A., Mönnich, W., Neumann, J., Arnold, J., and Heinecke, J., "Numerical Simulation of Maneuvering Combat Aircraft," *Notes on Numerical Fluid Mechanics and Multidisciplinary Design*, Vol. 92, Springer, Berlin, 2006, pp. 103–111.

[11] Galle, M., Gerhold, T., and Evans, J., "Technical Documentation of the DLR TAU code," DLR IB 233-97/A43, 1997.

[12] Gerhold, T., Galle, M., Friedrich, O., and Evans, J., "Calculation of Complex Three-Dimensional Configurations Employing the DLR TAU code," AIAA Paper 97-0167, Jan. 1997.

[13] Gerhold, T., "Overview of the Hybrid RANS Code TAU," edited by N. Kroll, and J. Fassbender, *MEGAFLOW: Numerical Flow Simulations for Aircraft*, Vol. 89, Springer, Berlin, 2005, pp. 81–92.

[14] Dwight, R. P., "Time-Accurate Navier–Stokes Calculations with Approximately Factored Implicit Schemes," *Computational Fluid Dynamics 2004*, Pt. 5, Springer, Berlin, 2006, pp. 211–217.

[15] Madrane, A., Raichle, A., and Stürmer, A., "Parallel Implementation of a Dynamic Overset Unstructured Grid Approach," *Proceedings of the Third International Conference on Computational Fluid Dynamics, ICCFD3*, European Community on Computational Methods in Applied Sciences, Regensburg, Germany, 2004.

[16] Mönnich, W., and Buchholz, J. J., "SIMULA - Ein Programmpaket für die Simulation dynamischer Systeme - Dokumentation und Benutzeranleitung," Ver. 2, DFVLR Institutsbericht IB 111-91/28, 1991.

[17] Hoffmann, D., Neumann, J., and Sinapius, M., "Strukturmechanische Identifikation von Halterung und Windkanalmodell AeroSUM," DLR IB 232-2002-C06, 2002.

[18] Neumann, J., "Strukturmechanische und strukturdynamische Finite Element Modelle des Windkanalmodells AeroSUM mit Halterung," DLR IB 232-2003-J01, 2003.

[19] Arnold, M., and Vaculin, O., "Multibody System Simulation in Vehicle System Dynamics," *Vehicle System Dynamics* (Special issue in memory of Professor Willi Kortüm), Vol. 41, No. 5, 2004, pp. 335–429. doi:10.1080/00423110412331300318

[20] "MpCCI Mesh Based Parallel Code Coupling Interface. Specification of MpCCI," Ver. 2.0, Fraunhofer Inst. for Algorithms and Scientific Computation, Sankt Augustin, Germany, 2003, http://www.mpcci.de/.

[21] Arnold, J., Einarsson, G., and Schütte, A., "Multibody Simulation of an Aeroelastic Delta Wing in Roll Manoeuvres," *Proceedings of the 25th Congress of the International Council of the Aeronautical Sciences*, International Council of the Aeronautical Sciences, Hamburg, 2006.

[22] Farhat, C., and Lesoinne, M., "Higher-Order Staggered and Subiteration Free Algorithms for Coupled Dynamic Aeroelasticity Problems," AIAA Paper 98-0516, 1998.

[23] Neumann, J., "Multidisziplinäre Simulation eines rollenden, generischen Deltaflügels-Kopplung von Aerodynamik, Flugmechanik und Strukturdynamik," *Proceedings, Deutscher Luft- und Raumfahrt-kongress 2005*, Friedrichshafen, Deutschland, 2005.

[24] Einarsson, G., and Neumann, J., "Multidisciplinary Simulation of a Generic Delta Wing: Aerodynamic, Flight-Dynamic and Structure-Mechanic Coupling," *CIMNE, Computational Methods for Coupled Problems in Science and Engineering*, 1st ed., CIMNE, Barcelona, Spain, 2005, ISBN 84-95999-71-4.

[25] Schulze, S., "Numerische Integration der aeroelastischen Bewegungs-gleichungen eines Flügelprofils," DLR IB 232-94 J 06, 1994.

[26] Beckert, A., and Wendland, H., "Multivariate Interpolation for Fluid-Structure-Interaction Problems Using Radial Basis Functions," *Aerospace Science and Technology*, Vol. 5, No. 2, 2001, pp. 125–134. doi:10.1016/S1270-9638(00)01087-7

[27] Schreiber, A., "The Integrated Simulation Environment TENT," *Concurrency and Computation: Practice and Experience*, Vol. 14, Nos. 13–15, 2002, pp. 1553–1568. doi:10.1002/cpe.676

[28] Rein, M., Höhler, G., Schütte, A., Bergmann, A., and Löser, T., "Ground-Based Simulation of Complex Maneuvers of a Delta-Wing Aircraft," *25th AIAA Aerodynamic Measurement Technology and Ground Testing Conference*, AIAA Paper 2006-3149, June 2006.

[29] Dol, H. S., Kok, J. C., and Oskam, B., "Turbulence Modeling for Leading-Edge Vortex Flows," AIAA Paper 2002-0843, Jan. 2002.

[30] Fritz, F., "RANS Solutions for the CAWAPI F-16XL in Solution Adapted Hybrid Grids," *45th AIAA Aerospace Sciences Meeting and Exhibit*, AIAA Paper 2007-492, Jan. 2007.